

Microwave signatures of ice hydrometeors from ground-based observations above Summit, Greenland

C. Pettersen¹, R. Bennartz^{1,2}, M. S. Kulie¹, A. J. Merrelli¹, M. D. Shupe³, and D. D. Turner⁴

[1]{Space Science and Engineering Center, Madison, Wisconsin}

[2]{Vanderbilt University, Nashville, Tennessee}

[3]{Cooperative Institute for Research in Environmental Science, University of Colorado and NOAA – Earth System Research Laboratory, Boulder, Colorado}

[4] {National Severe Storms Laboratory, Norman, Oklahoma}

Correspondence to: C. Pettersen (claire.pettersen@ssec.wisc.edu)

Abstract

Multi-instrument, ground-based measurements provide unique and comprehensive datasets of the atmosphere for a specific location over long periods of time and resulting data compliments past and existing global satellite observations. This paper explores the effect of ice hydrometeors on ground-based, high frequency passive microwave measurements and attempts to isolate an ice signature for summer seasons at Summit, Greenland from 2010 – 2013. Data from a combination of passive microwave, cloud radar, radiosonde, and ceilometer were examined to isolate the ice signature at microwave wavelengths. By limiting the study to a cloud liquid water path of 40 g/m^2 or less, the cloud radar can identify cases where the precipitation was dominated by ice. These cases were examined using liquid water and gas microwave absorption models, and brightness temperatures were calculated for the high frequency microwave channels: 90, 150, and 225 GHz. By comparing the measured brightness temperatures from the microwave radiometers and the calculated brightness temperature using only gas and liquid contributions, any residual brightness temperature difference is due to emission and scattering of microwave radiation from the ice hydrometeors in the column. The ice signature in the 90, 150, and 225 GHz channels for the Summit Station summer months was isolated. This measured ice signature was then compared to an equivalent brightness temperature difference calculated with a radiative transfer model

1 including microwave single scattering properties for several ice habits. Initial model results
2 compare well against the four years of summer season isolated ice signature in the high-
3 frequency microwave channels.

4 **1 Introduction**

5 Better characterization of precipitation in the Arctic is fundamental to improve our
6 understanding of the hydrological cycle and mass balance of the polar ice sheets. The
7 Greenland Ice Sheet (GIS) is of particular interest as it has relatively large impacts on the
8 Earth's climate system (Church *et al.*, 2001). Understanding the characteristics of
9 precipitation above the GIS is a key factor in quantifying the full energy and ice mass
10 balance. Accurate atmospheric measurements and remote sensing precipitation retrievals
11 from multiple instruments are essential to resolving and refining precipitation estimates over
12 the GIS.

13 Microwave radiometers (MWRs) are a common remote sensing instrument, which make
14 passive measurements of radiance at specific frequencies. Typically, MWR measurements are
15 used to retrieve atmospheric properties, specifically liquid water path and precipitable water
16 vapor (LWP and PWV, respectively). A frequently implemented technique for characterizing
17 ice hydrometers from satellites and aircraft is to use high-frequency microwave channels (89
18 GHz and greater) and look for depressed brightness temperatures due to scattering of the
19 upwelling radiation to calculate an ice water path (Hong *et al.*, 2005; Kulie *et al.*, 2009; Deter
20 and Evans, 2000). While liquid and gas in the atmospheric column absorb and emit
21 microwave radiation, ice hydrometeors scatter surface radiation away from the satellite sensor
22 and depress the observed brightness temperature (BT). The same technique can be used from
23 the ground looking up with the opposite effect, as ice scatters the upwelling radiation back
24 towards the MWR sensor. Kneifel *et al.* (2010; hereafter K10) demonstrated the presence of
25 an enhanced BT signature from ice hydrometeors in downwelling microwave radiance
26 observations for a case study of snowfall in the Alps using ground-based MWRs. The high-
27 frequency channels (90 and 150 GHz) are considered "window channels", since these
28 frequencies are free of strong gas absorption lines. At these frequencies the clear sky
29 downwelling radiance is very small, so when ice or liquid water is present these channels see
30 a warmer BT, as seen by the K10 study.

31 If there are ice hydrometeors present in the atmosphere column, they will have two effects on
32 the observed downwelling radiance at the surface: emission of radiation and scattering of the

1 surface-emitted radiation back to the instrument. In general, ice hydrometeors have fairly high
2 single scatter albedo (SSA) at high microwave frequencies, regardless of habit and size
3 distribution. Typically the SSA will be in the range 0.8-0.9 (Liu, 2008), which implies that
4 scattered radiation is likely the larger effect, but there may still be significant emitted
5 radiation from the ice hydrometeors. Since some of the ice signature is scattered surface
6 radiation, the magnitude of the effect is related to both the surface temperature and emissivity.
7 The surface emissivity of different types of snow seen at Summit varies in the range of 0.60 to
8 0.91 for the higher frequency passive microwave channels used in this study (Yan *et al.*,
9 2008). This makes the ice signature challenging to model because it depends on both
10 properties of the ice hydrometeors (habit, size distribution, amount, etc.) and the surface
11 (temperature, roughness, emissivity).

12 We propose that the enhanced BT from the ice hydrometeors can be isolated and quantified
13 by combining the observed data from instruments in the Integrated Characterization of
14 Energy, Clouds, Atmospheric State, and Precipitation at Summit project (ICECAPS; Shupe *et al.*, 2013)
15 with radiative transfer models of the gas and liquid in the atmosphere. By doing
16 this we are enhancing the K10 study by expanding it to multiple years of data in an Arctic
17 environment with very low amounts of liquid water and precipitable water vapor, which
18 present unique challenges. Additionally, since the temperatures at Summit Station are below
19 freezing, we are implementing a newly developed cloud liquid water model for more accurate
20 retrievals in the presence of supercooled water (Kneifel *et al.*, 2014; Turner *et al.*, 2015).
21 Because the ice signature is also dependent on ice crystal habit and size distribution, relying
22 on a small number of precipitation events to derive the ice signature may bias the result
23 toward specific precipitation situations. The large dataset from the ICECAPS Project allows
24 for the average ice signature to be computed over many precipitation events, thus reducing
25 this potential sampling bias.

26 In this paper we use the ICECAPS instrument suite (described in Sect. 2) to resolve a signal
27 from the ice hydrometeors present in the high frequency, ground-based MWRs (90, 150, 225
28 GHz) for multiple years of summer season data at Summit, Greenland. We modeled the gas
29 and liquid present in the column and compared that to observations from the MWRs (Sect. 3).
30 We had to develop a technique to accurately model the absorption/emission from the liquid
31 water and atmospheric gases; this is described in Sect. 4. Finally, we demonstrate an initial
32 scattering model of the ice and compare these results to the observed signature (Sect. 5).

1 **2 Datasets and methods**

2 Studying the seasonal characteristics of the ice hydrometeors above the GIS is made possible
3 with observations from the ICECAPS instrument suite from 2010 to 2013. Model results are
4 then combined or compared with observations from specific instruments in the ICECAPS
5 suite.

6 **2.1 ICECAPS project and instrument suite**

7 Summit Station was the site of the Greenland Ice Sheet Project 2 (GISP2) ice core project,
8 and has been expanded to a continuously operational science facility dedicated to studying the
9 atmosphere and ice sheet properties of the GIS (Dansgaard *et al.*, 1993). Summit Station is
10 home to many atmospheric and snow science instruments, including ICECAPS, which is
11 purposely co-located at Summit Station to aid in understanding the cloud and atmosphere
12 properties over the GIS and their interaction with the cryosphere. Since 2010, the ICECAPS
13 suite of instruments has been monitoring a variety of atmospheric parameters to further our
14 knowledge of atmospheric processes above the GIS (Shupe *et al.*, 2013). The ICECAPS
15 project will remain at Summit until at least 2018, thus providing a comprehensive dataset and
16 analyses of the atmosphere over central Greenland. Additionally, ICECAPS is expanding the
17 network of past and existing high-latitude atmospheric suites (i.e., Eureka, Canada and
18 Barrow, Alaska, Ny‘Alesund) already helping to characterize Arctic atmospheric and cloud
19 processes (Shupe *et al.*, 2011; Uttal *et al.*, 2015).

20 ICECAPS is modeled after other successful Arctic observatories and is similar in scope to
21 facilities run by the Department of Energy’s Atmospheric Radiation Measurement (ARM)
22 Program (Ackerman *et al.*, 2003; Shupe *et al.*, 2013). The ICECAPS instrument suite is
23 supported by year-round technicians and support staff at Summit Station and is updated with
24 new instruments, upgrades, and repairs by researchers every summer. Table 1 illustrates a
25 brief overview of the ICECAPS instruments used in this study, including key specifications,
26 measurements, and retrieved parameters. We employed data from a subgroup of the
27 ICECAPS suite and a co-located 225 GHz MWR. The available measurements and retrieved
28 values are further described in the following sections.

1 2.1.1 Millimeter cloud radar

2 The Millimeter wavelength Cloud Radar (MMCR) is a zenith pointing, 35 GHz (Ka band)
3 radar with processed measurements provided every ten seconds at a height resolution of 45
4 meters (Moran *et al.*, 1998). The MMCR measures the profile of reflectivity, Doppler
5 velocity, and Doppler spectral width in the column above. For the MMCR, hydrometeors
6 with geometric diameters less than approximately 3 mm are in the Rayleigh scattering region
7 (Kneifel *et al.*, 2011). However, for ice hydrometeors larger than ~3 mm diameter the
8 Rayleigh approximation breaks down (at this size, the MMCR starts to see Mie resonance
9 effects) and the backscatter cross-section depends on ice habit (Kneifel *et al.*, 2011; Petty and
10 Huang, 2010).

11 The Doppler velocity measures the fall speed of particles toward the radar – this is dependent
12 on the mass and projected area of the ice hydrometer population, thus some microphysical
13 insight is gained from these fall speed values. However, the particles are embedded with a
14 vertical wind field that will affect the measured fall speed.

15 Finally, the variance of the velocity in a given pulse volume, the Doppler spectral width, aids
16 in determining turbulence and contains indicators of hydrometeor phase. Strong turbulence or
17 multiple phases/habits in a cloud layer leads to large Doppler spectral width. On the other
18 hand, uniform particle populations, such as for those precipitating out of a cloud, exhibit
19 relatively low Doppler spectral width. By combining these measured quantities from the
20 MMCR, we can infer many properties of the hydrometeors observed at Summit.

21 2.1.2 Microwave radiometers

22 ICECAPS also gathers observations from three different passive MWRs all built by
23 Radiometer Physics GmbH. The Humidity and Temperature Profiler (HATPRO) has seven
24 channels from 22-32 GHz (near 22.24 GHz water vapor absorption line) and seven channels
25 from 51-58 GHz (near oxygen absorption line; Rose *et al.*, 2005). The high-frequency
26 microwave MWR (MWRHF) has two high-frequency channels: 90 and 150 GHz. The two
27 radiometers are run in a master-slave configuration and make coincident measurements every
28 four seconds. Data from the third co-located MWR, which is sponsored by the Academia
29 Sinica Institute of Astronomy and Astrophysics (ASIAA) group, observes downwelling
30 radiation at 225 GHz and takes measurements every 4 seconds (Matsushita *et al.*, 2013).

1 Although all of the MWRs measure the downwelling atmospheric radiance at several
2 elevation angles, in this study we only use data from zenith pointing.

3 Passive microwave radiometry is commonly used to derive liquid water path (LWP; Crewell
4 *et al.*, 2009). By combining the BTs observed from specific channels, precipitable water
5 vapor (PWV) and LWP are derived. Historically, LWP and PWV at ARM sites are derived
6 using the 23.84 and 31.40 GHz channels using a version of the MWR Retrieval (MWRRET)
7 algorithm (Turner *et al.*, 2007a). The physical retrieval method employs the MonoRTM
8 radiative transfer model (Clough, *et al.* 2005) and the Liebe91 liquid water model (Liebe,
9 1991). It was found that the addition of high frequency channels to the retrieval algorithm
10 improves LWP accuracy, particularly for low LWP amounts. By adding the 90 GHz channel,
11 the uncertainty is reduced from 20 – 30 g/m² to better than 12 g/m² (Crewell *et al.*, 2003;
12 Löhnert *et al.*, 2003). The four channel MWRRETv2, which includes the addition of the 90
13 and 150 GHz channels, calculates an uncertainty of 4-5 g/m² for typical retrievals at Summit
14 (MWRRETv2).

15 The reduced uncertainty at low LWPs is important to this study, as the cloud liquid water path
16 on average at Summit (and the Arctic as a whole) is small as 80% of liquid-bearing clouds in
17 the Arctic have less than 100 g/m² LWP (Turner *et al.*, 2007b). However, the K10 study
18 showed that high-frequency channels have enhanced brightness temperatures when ice is
19 present in the column. Additionally, recent studies have indicated that many liquid water
20 absorption models do a poor job adequately accounting for supercooled cloud liquid water
21 (Turner *et al.*, 2015; hereafter TKC15). We compared results from four channel
22 MWRRETv2 retrievals using both the Liebe91 and TKC15 models. We found that the
23 MWRRET retrieval had improved convergence when using TKC15 versus the Liebe91 cloud
24 liquid water model, especially in the difficult to resolve ice affected cases. To further
25 mitigate the effect of the enhanced BTs in the high frequency channel, we opted to use
26 MWRRETv2 with the TKC15 model and only three channels to compute LWP and PWV:
27 23.84, 31.40, and 90 GHz. Due to computational expense, the MWRRET retrieval is run on
28 the MWR data every 100 seconds.

29 2.1.3 Ceilometer

30 The MWRRET retrieval gives the integrated cloud liquid water amount but no information
31 about cloud altitude. Cloud base height (CBH) is estimated from a Vaisala Ceilometer

1 (VCEIL). The VCEIL is a vertically pointing 905 nm pulsed laser system with 15 meter
2 height resolution and takes a measurement every 15 seconds. Cloud base heights (up to three
3 layers) are determined based on the backscattered signal received by the instrument. We use
4 the first cloud base height retrieved from the VCEIL to define the base of the cloud liquid
5 water layer in this study.

6 2.1.4 Radiosondes

7 This study also uses data from twice daily balloon-borne radiosondes (manufactured by
8 Vaisala, models RS-92K and RS-92SGP) launched at Summit Station. The launches occur at
9 approximately 1200 and 2400 Coordinated Universal Time (UTC), and gather *in-situ*
10 measurements of temperature, pressure, relative humidity, and, in some cases, horizontal wind
11 speed and direction. These thermodynamic profiles provide critical input for the radiative
12 transfer modeling (see Sect. 2.2).

13 2.1.5 Merged Data

14 The datasets described above are merged together to a common sampling time, defined by the
15 MWRRET retrieval (every 100 seconds). The slower datastream (twice daily radiosonde) is
16 linearly interpolated to the common sampling time, and the faster datastreams are simply
17 subsampled at the MWRRET retrieval times. We interpolate all the data to the fixed height
18 grid defined by the MMCR.

19 For an example day, we use data from the prior day's radiosonde launch (day -1, 2400 UTC)
20 along with the two radiosondes launched for the given day (1200 and 2400 UTC) and linearly
21 interpolate the temperature, pressure, and relative humidity of each layer in the column
22 throughout the day to the MWRRET temporal grid. The vertical layering uses the MMCR
23 vertical grid up to 7.5 km altitude above ground level (AGL). Above this altitude, the layering
24 becomes gradually coarser and extends to up 30 km AGL. Next, the MWR retrieved PWV is
25 used to scale the interpolated relative humidity from the radiosonde – this is because the PWV
26 retrieved value is higher temporal resolution and more accurate than the radiosonde data
27 (Turner *et al.*, 2003). Finally, a single layer cloud is inserted into the vertical grid at the first
28 cloud base height (CBH1) detected by the VCEIL, with the MWR retrieved LWP value.

1 **2.2 Absorption coefficients for gas and liquid water**

2 The emission and absorption of the gases and liquid water in the atmospheric column are
3 modeled using *in situ* observations of temperature and pressure and remotely sensed values of
4 integrated water vapor, liquid water content, and cloud base height from the ICECAPS
5 instruments. To compute the volume absorption coefficients of dry air and water vapor in the
6 atmospheric column, we employed the MonoRTM (v5.0; Clough, *et al.* 2005) using inputs of
7 layer temperature, pressure, and scaled water vapor. The liquid water absorption and
8 emission is modeled using the TKC15 Model (Turner *et al.*, 2015) with inputs of liquid water
9 content (LWC) at a defined cloud height and temperature. For altitudes above the radiosonde
10 profile, a subarctic standard atmosphere profile is assumed. The simulated emission is not
11 sensitive to the details of the upper atmosphere profile, but systematic biases would be present
12 if the atmosphere was artificially truncated at too low an altitude.

13 **2.3 Successive Order of Interaction radiative transfer model**

14 In ice cloud free atmospheres, the RT model need only consider the absorption and emission
15 of atmospheric gases and liquid water. When ice is introduced into the column, multiple
16 scattering can occur and we then must employ a radiative transfer model that accounts for
17 scattering. The Successive Order of Interaction (SOI) RT model accurately simulates
18 scattering for the infrared and microwave spectral region (Heidinger *et al.*, 2006; O'Dell *et*
19 *al.*, 2006). The SOI model combines the layer-averaged optical properties and temperature in
20 order to compute downwelling radiance at selected frequencies. The layer-averaged optical
21 properties are calculated from the gas and liquid water absorption models (described above)
22 and ice optical properties (further discussed in Sect. 5). The SOI modeled BTs can then be
23 compared to MWR observations. For all cases used in this study we employed the SOI
24 radiative transfer model, even when modeling non-scattering atmospheres that only include
25 gases and cloud liquid water absorption. As is further discussed in the subsequent section,
26 comparing the measured and modeled BTs at specific frequencies lends insight into the
27 hydrometers present in the atmospheric column.

28 **3 Ice hydrometeor behavior as observed by ICECAPS**

29 Similar to K10, we compared the BTs in the high frequency channels of the MWRs to the
30 output from the radiative transfer model calculation. The K10 study employed a radiative
31 transfer model that included absorption/emission and scattering to simulate the behavior of

1 the ice signature based on the habit, surface emissivity, etc. Different from K10, we do not
2 initially include an ice scattering model for the purpose of identifying the ice signature. We
3 instead attempt to isolate the ice radiative signature in the observations by accounting for any
4 other potential emission or absorption sources within the column. If we compare the
5 calculated BT using only gas and liquid water to the observed BTs from the MWRHF, any
6 difference should be due to the ice signature. Consequently, the average ice hydrometeor
7 radiative signature can be computed over many precipitation events by extending the analysis
8 to the full available ICECAPS dataset.

9 **3.1 Characterization of ice precipitation at Summit**

10 We can acquire statistics of different precipitation regimes at Summit by merging all available
11 MMCR data and plotting Contoured Frequency by Altitude Diagrams (CFADs). CFADs
12 depict all data as a two-dimensional occurrence histogram, with the vertical axis representing
13 the height dimension and the horizontal axis representing a radar measurement (for example,
14 reflectivity). Figure 1a is a CFAD of all the reflectivity values measured by the MMCR for
15 any given time within the summer months – June, July, August, (JJA) – 2010 through 2013.
16 We can highlight the types of hydrometeors observed during specific atmospheric conditions
17 by filtering the MMCR reflectivity CFAD, illustrated in Fig. 1a, as a function of other
18 ICECAPS instrument measurements or derived parameters.

19 Filtering the MMCR CFADs by the corresponding MWR-derived LWP for the same time
20 period can identify regimes in which ice hydrometeors are likely present. We partition the
21 data with a threshold LWP value in order to select cases that have low LWP. The exact
22 threshold value is arbitrary, as the resulting CFADs are not sensitive to the particular
23 threshold value. We tried values of 5, 10, and 40 g/m^2 and observed qualitatively similar
24 CFADs. We selected a 40 g/m^2 LWP threshold for the remaining analysis, since this yielded a
25 larger number of cases for the study (as opposed to the lower LWP threshold values).

26 As depicted in Fig. 1b and c, the MMCR reflectivity CFAD for JJA has been filtered by cases
27 when LWP was less than and greater than 40 g/m^2 , respectively. The resulting CFADs have
28 different characteristics from each other and lend insight to the behaviors of the hydrometeors
29 in each case. For the case of LWP less than 40 g/m^2 , the CFAD illustrates common ice
30 hydrometeor behaviors: a fall-streak like pattern of increasing reflectivity with decreasing
31 height and peak near-surface reflectivities above 0 dBZ (see Fig. 1b). In contrast, the

1 reflectivity CFAD for the cases where LWP is greater than 40 g/m^2 has a concentration of
2 counts at a broader range of smaller reflectivities located at lower altitude, likely indicating
3 dominance of shallow mixed ice and supercooled water cloud (though there is also a faint
4 signal indication of some fall-streak behavior; see Fig. 1c). The reflectivities shown in Fig.
5 1b for less than 40 g/m^2 LWP cases have characteristics of deep, precipitating ice cloud, while
6 the greater than 40 g/m^2 LWP cases show features similar to the shallow mixed-phase
7 stratocumulus (Fig. 1c). Additionally, Fig. 1 panels d through i, depict the Doppler velocities
8 and spectral width measurements from the MMCR as CFADs for all LWPs, less than 40 g/m^2 ,
9 and greater than 40 g/m^2 . The features seen in the Doppler velocity and spectral width
10 CFADs for the cases less than 40 g/m^2 are consistent with the characteristics of deep,
11 precipitating ice cloud (high fall speeds and low spectral widths throughout the column,
12 relative to greater than 40 g/m^2 LWP cases).

13 The frequency of cases in JJA where the LWP is greater than 40 g/m^2 is $\sim 22\%$, while the
14 cases where LWP is less than 40 g/m^2 is $\sim 63\%$ of the time, and clear sky is the remaining 15%
15 of cases (i.e., where the MMCR reflectivity is less than -60 dBZ). To maximize the likelihood
16 of observing ice dominated cases, we limit our work to focus on cases in JJA with LWP of
17 less than 40 g/m^2 . As stated above, the cases with LWP greater than 40 g/m^2 show features
18 consistent with the shallow mixed-phase stratocumulus and by filtering out some of these
19 events, we can better focus the study on the deeper, precipitating ice clouds. Since cases with
20 LWP of less than 40 g/m^2 represent the majority at Summit during the summer months, we
21 can use this filter to get an accurate characterization of ice hydrometeor behavior while
22 limiting interference from higher liquid water path.

23 We argue that the large radar reflectivity values are directly correlated to ice backscatter and
24 cannot be from liquid precipitation, as Summit is never above freezing and thus large liquid
25 hydrometeors (greater than $80 \mu\text{m}$ diameter) are highly unlikely to occur (Pruppacher and
26 Klett, 2000). Since we do not expect to see liquid hydrometeors larger than cloud droplets at
27 Summit Station, MMCR observed reflectivities greater than -15 dBZ should be indicative of
28 ice (Frisch *et al.*, 1995).

29 **3.2 Enhanced brightness temperatures in the high frequency channels**

30 As postulated from previous case studies in K10, the higher frequency channels in the
31 ground-based zenith-pointing MWRs will see an enhanced BT in the presence of ice in the

1 column. Thus, we examine the difference between the measured BTs from the 90 and 150
2 GHz channels and the SOI model outputs (with no ice included, gas and liquid water
3 contributions only) at that same frequency. As illustrated in the contour plot of the JJA
4 comparison in Fig. 2c and d, there is an increase in the difference of the observed minus
5 modeled BTs as a function of the MMCR reflectivity converted to what we refer to as
6 “ Z_{PATH} ”, though very small in the 90 GHz channel.

7 The Z_{PATH} is simply the column integrated reflectivities with units of mm^6/m^2 . This MMCR
8 Z_{PATH} measurement is related to the total amount of hydrometeor backscatter in the
9 atmospheric column. The use of Z_{PATH} is advantageous because it acts as a proxy for ice
10 water path (IWP) yet does not rely on conversions that are sensitive to ice habit (Kulie *et al.*,
11 2010). Z_{PATH} is defined as:

$$12 \quad Z_{\text{PATH}} = \int 10^{0.1 \cdot R(z)} dz . \quad (1)$$

13 Where $R(z)$ is the observed radar reflectivity profile in units of dBZ.

14 The observed minus modeled BT differences at 90 and 150 GHz have a clear positive
15 dependence on Z_{PATH} . As stated in the previous section, we do not expect to see any liquid
16 hydrometeors at reflectivities greater than -15dBZ at Summit since there is no “warm rain”
17 process, which means that large Z_{PATH} values are indicative of ice. Therefore, the relationship
18 between the BT differences at 90 and 150 GHz and the MMCR Z_{PATH} suggest that the
19 enhanced BT signature is caused by ice hydrometeors.

20 **3.3 Depressed brightness temperatures at 31.40 GHz**

21 The lower frequency channels (23.84 and 31.40 GHz) should exhibit little to no effect from
22 the presence of ice hydrometeors in the atmospheric column, as the microwave radiation at
23 these frequencies is comparatively insensitive to ice hydrometeors (Johnson *et al.*, 2012).
24 Thus we expect the histogram contours to be nearly vertical at the 23.84 and 31.40 GHz for
25 the relationship between the BT differences and the integrated reflectivity (Z_{PATH}). However,
26 as seen in Fig. 2b, the 31.40 GHz channel shows a clear negative dependence on Z_{PATH} at the
27 highest values. There is no physical mechanism by which ice hydrometeors could decrease
28 the observed downwelling radiance. This result implies an issue with the input values
29 implemented in the radiative transfer model, as it is unlikely for the low frequency channels at
30 23.84 and 31.40 GHz to see much contribution from ice in the column.

1 Two of the inputs for the radiative transfer model are retrieved values based on BTs from the
2 MWRs: the PWV and LWP. As explained in Sect. 2.1.2., the retrieval for the PWV and LWP
3 employ a three-channel algorithm, which includes the 90 GHz channel. Though we tried to
4 mitigate the effect of the ice by using the three channel algorithm, the enhanced BT in the 90
5 GHz still has a significant impact on the retrieved LWP and PWV. More precisely, the
6 retrieval will tend to adjust the LWP and PWV in order to account for the enhanced BT from
7 the ice hydrometeors, leading to an overestimate of LWP and underestimate of PWV.

8 **4 Liquid water path retrieval influenced by ice**

9 As postulated in the previous section, we believe that the MWR retrieved LWP (PWV) values
10 are biased high (low) when a significant ice signature is present in the column due to the
11 retrieval incorporating the 90 GHz MWR channel. However, if we use only a retrieval based
12 on the lower frequencies of 23.84 and 31.40 GHz, the random error in LWP increases
13 dramatically to 20 – 30 g/m², which is a large fractional error (>50%). Thus, a relationship
14 for the LWP and PWV biases in the three-channel retrieval as a function of the MMCR
15 derived Z_{PATH} must be determined to accurately distinguish the ice signature. We developed a
16 first-order correction of the estimated MWRRET retrieval biases, where the intention of this
17 correction is to recover the ice signature, not to produce a formal correction to the ice-
18 influenced LWP and PWV retrievals.

19 **4.1 Ice signature influence on retrieved liquid water**

20 As illustrated in Fig. 2, the difference between measured and modeled BTs as a function of
21 Z_{PATH} , analogous to the amount of ice in the column, decreases in the 31.40 GHz. This effect
22 is an artifact in the simulated BTs caused by the following chain of events:

- 23 1. The presence of ice increases the observed BTs at 90 GHz but has little effect on the
24 lower frequencies.
- 25 2. Since the retrieval does not include effects from ice, the retrieval accounts for this
26 enhanced signal in the 90 GHz channel by increasing (decreasing) the retrieved LWP
27 (PWV) thus producing a positively (negatively) biased LWP (PWV) estimate.
- 28 3. Since the spectral absorption for the three water states (vapor, liquid, ice) have
29 different shapes, the retrieval cannot reduce the modeled-measured BT bias to zero for
30 all channels.

1 To better illustrate this idea it is useful to look at Fig. 2 from K10, where the optical thickness
2 as a function of frequency is plotted for several absorption models – for example, water
3 vapor, liquid water, ice by habit, etc. The liquid water and ice total optical depths (τ) are less
4 than 0.2 for these frequencies. Since the total τ is low, we can make two simplifying
5 approximations: first, the transmission to any atmospheric layer in the column is nearly 1; and
6 second, the change in transmission through a layer is approximately the change in τ for that
7 layer. This implies the BTs are a linear combination of τ for each atmospheric component.

8 The bias in the simulated BT, shown in Fig. 2, suggests that the MWRRET retrieved PWV
9 and LWP may be influenced by the presence of ice hydrometeor signature in the 90 GHz
10 channel used in the retrieval. Since the MWRRET does not include ice hydrometeors in the
11 radiative transfer calculation, it can only fit retrieval channel observations by adjusting the
12 PWV and LWP. The higher optical depth for liquid water at 90 GHz suggests that MWRRET
13 adds extra LWP to account for the observed microwave ice signature. This will increase the
14 forward modeled BT for the 23.84 and 31.40 GHz channels as well. Since there will be
15 effectively zero ice signature at the low frequency MWR observations, the extra LWP will
16 cause the low frequency BTs to be biased high. The retrieval partially compensates for the
17 high BT bias at low frequencies by decreasing the PWV, which will reduce the simulated BT
18 primarily at the 23.84 GHz channel, which is near the water vapor absorption line. Figure 3
19 shows these biases in a schematic fashion. Because the liquid absorption model uses the
20 MWR retrieved LWP and PWV as inputs to the SOI, a correction for the retrieved LWP and
21 PWV in the presence of ice is necessary to accurately quantify the ice impact on passive
22 microwave BTs.

23 **4.2 Ice influenced liquid water path correction**

24 The lower frequency channels are comparably insensitive to ice (Johnson *et al.* 2012), so we
25 focus on the 23.84 and 31.40 GHz channels to derive a first-order estimate for the MWRRET
26 LWP and PWV biases from the ice signature. In order to correct for the apparently biased
27 PWV and LWP, we make an ad-hoc linear correction to the retrieved values. We assume the
28 PWV and LWP bias are linearly related to the Z_{PATH} . As described in the previous section, the
29 channels used in the retrieval, the RT is in the linear regime. Thus, the PWV and LWP biases
30 are linearly related to biases in the forward modeled BT, with their relationships described by
31 the forward model Jacobian (\mathbf{K}). Formally, we if write the coefficients relating the Z_{PATH} and
32 the retrieval bias as e_{LWP} and e_{PWV} , then the forward model perturbation can be expressed as:

$$\begin{bmatrix} \delta\text{TB}_{23.84\text{GHz}} \\ \delta\text{TB}_{31.4\text{GHz}} \end{bmatrix} = \begin{bmatrix} K_{23.84\text{GHz, PWV}} & K_{23.84\text{GHz, LWP}} \\ K_{31.4\text{GHz, PWV}} & K_{31.4\text{GHz, LWP}} \end{bmatrix} \begin{bmatrix} e_{\text{LWP}} Z_{\text{PATH}} \\ e_{\text{PWV}} Z_{\text{PATH}} \end{bmatrix} \quad (2)$$

or:

$$\delta\text{TB} = \mathbf{K} e Z_{\text{PATH}} \quad (3)$$

Inverting Eq. 3 to solve for the e coefficients yields:

$$\mathbf{e} = \mathbf{K}^{-1} \delta\text{TB} \frac{1}{Z_{\text{PATH}}} \quad (4)$$

The linear relationship between δTB and Z_{PATH} can then be estimated from Fig. 4a and c, by measuring the slope of the point distribution. For the 23.84 GHz result, the slope is zero, which is due to compensating errors in LWP and PWV. For 31.40 GHz, the slope is approximately -3.3×10^{-4} K per (mm^6/m^2). Inserting these values into equation 4 yields a value of -1.3×10^{-4} g/m² per (mm^6/m^2) for e_{LWP} and 4.4×10^{-6} cm per (mm^6/m^2) for e_{PWV} .

To utilize these corrections in our modeling framework, the Z_{PATH} from the MMCR is multiplied by the scaling factor, and the PWV and LWP are adjusted accordingly (for example, for a Z_{PATH} of 10^4 mm⁶/mm², the correction would reduce the LWP by 1.3 g/m² and increase the PWV by 0.044 cm):

$$LWP_{\text{corrected}} = LWP_{\text{retrieved}} + e_{\text{LWP}} \times Z_{\text{PATH}} \quad (5)$$

$$PWV_{\text{corrected}} = PWV_{\text{retrieved}} + e_{\text{PWV}} \times Z_{\text{PATH}} \quad (6)$$

The corrected PWV and LWP are then used in the forward RT simulation with the SOI framework.

Returning to Fig. 3, we show the effect of these corrections for a standard profile at Summit with 0.1 cm PWV and 20 g/m² LWP. The top panel (a) shows the simulated downwelling microwave radiance spectrum with no ice included in the simulation, and the simulated spectrum with the biased PWV and LWP obtained by the retrieval. The second panel (b) shows the same simulated data after subtracting the simulated spectrum with no ice. The effect of the biased LWP and PWV on the microwave spectrum are shown independently (blue and green lines, respectively) and combined (cyan line). The residuals that are minimized by the retrieval (observed radiance minus forward model radiance) are the differences between the cyan line and the black “X”s. We see the compensating biases at

1 23.84 GHz, which minimizes the magnitude of the residuals at 23.84 GHz, as well as the
2 opposite signs for the residuals at 31 GHz (negative) and 90 GHz (positive). The cyan line
3 represents the retrieval's solution to minimizing the residuals when it cannot correctly account
4 for the ice signature, which impacts the observations from high frequency microwave channel
5 (90 GHz).

6 Comparison of the MWR observed data with the radiative transfer model – using the LWP
7 and PWV corrections for ice – for the JJA season from 2010 through 2013 for LWP of less
8 than 40 g/m^2 in the 23.84 and 31.40 GHz channels are insensitive with respect to the
9 integrated reflectivity (as seen in Fig. 4b and d). This correction is successful in removing the
10 high (low) LWP (PWV) incorporated from the ice signal, as the 31.40 GHz channel
11 comparison shows no dependence on moderate values of Z_{PATH} . With this successful
12 evaluation of the ice influenced LWP and PWV, we can rerun the model on the other
13 channels and characterize the signature from the ice hydrometeors because e_{LWP} and e_{PWV} are
14 frequency independent.

15 **5 Observed Brightness temperature differences from ice**

16 We present the LWP and PWV corrected results for the 23.84, 31.40, 90, and 150 GHz
17 channels. The lower frequency MWR channels exhibit insensitivity to the ice (Fig. 4b and d),
18 while the higher frequency MWR channels exhibit enhanced BTs when ice is present (Fig. 5).
19 Additionally, we present data from a co-located 225 GHz MWR, which exhibits even larger
20 BT differences with respect to the ice. Finally, we recast the results from these five MWR
21 channels and compare them to each other. We also show preliminary results from a simple
22 radiative transfer simulation as a first-order comparison of modeled results against the MWR
23 observed ice signature enhanced BTs in the 90, 150, and 225 GHz channels.

24 **5.1 Brightness temperature differences with corrected LWP and PWV**

25 All data presented are events in JJA with LWP of less than 40 g/m^2 . The measured MWR
26 observations are compared to the radiative transfer model including the LWP and PWV
27 corrections for ice. The results for the lower frequency channels, shown in Fig. 4b and d, no
28 longer depend on the Z_{PATH} – they should be insensitive to ice for most Z_{PATH} . In the high
29 frequency channels, 90 and 150 GHz, there is clear relationship between BT difference and
30 Z_{PATH} indicative of ice enhanced BTs (Fig. 5a and b). At the highest observed Z_{PATH} values

1 (about $10^5 \text{ mm}^6/\text{m}^2$), BTs are enhanced anywhere from 3 – 7 K in the 90 GHz channel and 10
2 – 30 K in the 150 GHz channel.

3 **5.2 Brightness temperature differences at 225 GHz**

4 Co-located with the ICECAPS measurements is the ASIAA a very high frequency MWRHF-
5 225, which allows us to extend this study to include a 225 GHz channel. As the effect of ice
6 on this frequency from ground observations has not yet been explored, the observed ice effect
7 in the 225 GHz channel is a new application of this instrument. As expected, the 225 GHz
8 exhibits a large BT enhancement due to ice (Fig. 5c). The MWRHF-225 was deployed in mid
9 2011, so the dataset is somewhat smaller than the ICECAPS dataset already described. In
10 addition, the MWRHF-225 does have slightly different time coverage (e.g., the instrument
11 downtime and QC flags are disjoint from the HATPRO and MWRHF). The dataset with all 5
12 MWR channels covers only the union where all instruments collected good data. At the
13 highest Z_{PATH} values within the combined datasets in JJA from 2011 to 2013, the 225 GHz
14 has enhanced BTs of up to 50 K at the highest Z_{path} . The 225 GHz results continue the trend
15 seen in the other high frequency channels (150 and 90 GHz): the Z_{PATH} value above which the
16 BT enhancement occurs appears to decrease as the MWR frequency increases, implying
17 increased sensitivity to the ice (Fig. 5).

18 **5.3 Multi-frequency comparison of brightness temperatures differences**

19 By plotting the difference in the observed minus calculated BTs in the MWR channels as a
20 function of each other, one may gain insight about the spectral character of the ice signature
21 in the microwave. Figure 6 depicts the BT difference of four of the MWR channels with
22 respect to that of the 90 GHz: 23.84, 31.40, 150, and 225 GHz. Additionally, the binned
23 values of the BT differences are colored by logarithm of the average Z_{PATH} within the bin,
24 thus, providing a visual reference for the relative ice amount.

25 In the top of Fig. 6 (panels a and b), the 23.84 and 31.40 GHz BT differences are plotted and
26 binned on the y-axis versus the values for the 90 GHz. Though the Z_{PATH} values increase as a
27 function of the difference in BT in the 90 GHz, both the 23.84 and 31.40 GHz have the same
28 Z_{PATH} values throughout most cases (i.e., the Z_{PATH} is neutral in the y-axis for all but the
29 highest Z_{PATH}), which is expected as the lower frequency channels are comparatively
30 insensitive to the ice. However, in panel c of Fig. 6, the observed enhanced BT at 150 GHz is

1 plotted versus the 90 GHz and there is an approximately linear relationship between the ice
2 effects at the two frequencies – with a slope of about 4 K BT difference in 150 GHz for every
3 1 K in 90 GHz. For both the 90 and 150 GHz, as the difference in the BT increases the Z_{PATH}
4 values do as well (though the 150 GHz is more sensitive to the Z_{PATH} than the 90 GHz and
5 therefore the effect of the BT enhancement occurs at a lower Z_{PATH} value). In the last plot in
6 Fig. 6 (panel d), we compare the enhanced BT values in the 225 GHz channel to those in 90
7 GHz and again have a linear relationship between the ice effects in the two channels.
8 Additionally, the slope of the 225 versus the 90 GHz BT differences is steeper than the 150
9 versus 90 GHz – for every 1 K in 90 GHz, there is a corresponding 10 K difference in the 225
10 GHz. As with the 90 and 150 GHz case, the 90 and 225 GHz multi-frequency plot shows
11 increasing Z_{PATH} values as a function of larger BT differences in both channels.

12 **5.4 Comparison of ice signatures observed with scattering model results**

13 Now that we have an estimate of the passive microwave ice signature, we can compare to
14 modeled results with our SOI framework, described in Sect. 2.3. We can find the difference
15 in modeled BTs in the presence of ice using SOI by running the model twice: once including
16 ice with contributions from the atmospheric gases and once with only the gases. The
17 difference between these two runs produce differences in BTs that allow for direct
18 comparison with our multi-frequency results (Fig. 6), and an assessment of the ice microwave
19 optical property models for the ice hydrometeors at Summit, Greenland.

20 For a first-order ice habit study, we used the temperature-dependent ice particle size
21 distribution parameterization from Field *et al.* 2007 (hereafter F07) for the particle size
22 distribution (PSD), which is developed from airborne stratiform ice cloud in-situ
23 measurements in the midlatitudes. Additionally, we used information from the Liu database
24 of microwave single-scattering properties for three-bullet rosettes (LR3), sectored snowflakes
25 (LSS), and dendrites (LDS) for ice habit characteristics (Liu, 2008; note that these are the
26 same ice habits used in the K10 study). The PSD, ice habit, and radar backscatter cross-
27 section information are used to convert the MMCR reflectivity measurements to ice water
28 content (IWC). This IWC is then recombined with the PSD and ice habit information and the
29 microwave optical properties at the specific MWR frequencies, yielding the layer optical
30 properties needed to simulate the passive MWR measurements (see Kulie *et al.*, 2010 for
31 further details). The SOI model uses these layer optical properties to calculate BTs at MWR

1 frequencies. Finally, the emissivity of the snow surface is assumed to be 0.6, consistent with
2 Yan *et al.* (2008) based on common snow surface conditions at Summit Station.

3 For an initial test of the model, we generate a synthetic 1 km thick ice cloud with a range in
4 MMCR Z_{PATH} ($10^3 - 10^5 \text{ mm}^6/\text{m}^2$), inserted at 1-2 km above Summit in a temperature and
5 water vapor profile typical for summer months at the site. We make no distinction between
6 precipitating ice and cloud ice in these simulations. The MMCR derived Z_{PATH} is evenly
7 distributed throughout the 1 km synthetic cloud. No liquid water cloud was included. The
8 SOI modeled ice results with respect to the multi-frequency observations are shown in Fig. 7.
9 The modeled LDS, LSS, and LR3 ice habits are over-plotted on the observations and show a
10 similar slope for both the 150 versus 90 GHz and the 225 versus 90 GHz cases (panels a and
11 b, respectively). Though the slope is similar, the equivalent Z_{PATH} values for the simulations
12 show slightly larger BT differences than those seen in the measurements.

13 The small differences between the SOI model results and the observations with regard to
14 equivalent Z_{PATH} may stem from the ice habit assumptions and/or the PSD used for these
15 initial results. First of all, we can run SOI for only a single habit at a time and the model runs
16 for these habits should bound the observations if assumptions made for the PSD are correct.
17 The F07 parameterization may not adequately represent PSDs at Summit as this
18 parameterization is derived from midlatitude flight campaign measurements of ice stratiform
19 clouds and may very well be not at all applicable to the arctic (Field *et al.*, 2005; 2007).
20 Additionally, the F07, parameterization assumes a particle mass-size relationship appropriate
21 for aggregated ice particles, while non-aggregated, pristine ice crystals are commonly
22 observed at Summit (Shupe *et al.*, 2013). Furthermore, the temperatures observed in the F07
23 parameterization are much higher than those at Summit and therefore the growth mechanisms
24 of the ice hydrometeors in this PSD may be different than those in the Arctic. Future work
25 will explore other PSDs and particle size relationships, which will aid our understanding of
26 the ice habits at Summit. A recent installation of a Multi-Angle Snowflake Camera (MASC;
27 Garrett *et al.*, 2012) to ICECAPS will gather more information on ice habits.

28 **5.5 Future work on the LWP and PWV estimate in the presence of ice**

29 The above results are based on our first-order assessment of the ice-influenced LWP and
30 PWV biases. Our current correction is defined in terms of the three-channel MWRRET
31 retrieved LWP. As noted in Sect. 2.1.2, this retrieval is used for this study as it is more

1 sensitive to and has better precision for low LWPs. One possible BT correction can be
2 estimated by examining specific “dry snow” cases (i.e., extremely low LWP and high Z_{PATH}),
3 and by using the results from the present analysis. Additionally, we can compare these “dry
4 snow” cases with independent LWP measurements using the mixed-phase cloud property
5 retrieval algorithm (MIXCRA; Turner, 2007c). By using the TKC15 liquid water absorption
6 model in MWRRET, which is more spectrally accurate at cloud liquid water temperatures
7 below 0°C, we were able to recover many high Z_{PATH} cases that we found were previously
8 discarded using the Liebe91 model. We believe that using TKC15 over the Liebe91 model
9 reduced some of the small bias errors in our method and is a more appropriate choice for
10 modeling cloud liquid water at Summit. Ultimately, the goal would be to create a coincident,
11 multi-instrument retrieval of the LWP, PWV, and IWP under all atmospheric conditions.

12 **6 Conclusions**

13 This study first examined cloud and precipitation statistics derived from the MMCR and
14 partitioned the data with a specified LWP derived from the MWR. By limiting our study to
15 low LWP (less than 40 g/m²), we identify likely precipitating cases and then compared MWR
16 BT observations against modeled BT contributions from gas and liquid components. This
17 comparison enabled us to isolate a signature from the precipitating ice in the high-frequency
18 MWR channels. The enhanced BT at the 90, 150, and 225 GHz is the ice signature for the
19 majority of precipitating cases at Summit Station for the summer seasons of 2010 – 2013.

20 We identified a bias in the current MWRRET retrieved LWP and PWV caused by the ice
21 signature and utilization of 23.84, 31.40, and 90 GHz channels as part of this study, and
22 developed and applied a first-order correction (described in Sect. 4). The bias correction to
23 the three-channel retrieval is not the focus of this study, but had to be addressed to quantify
24 the ice signature in at microwave frequencies. Overall, the LWP and PWV bias due to ice
25 occurs in a small fraction of the total data, and is relatively small in magnitude. For example,
26 the high Z_{PATH} ($>10^4$ mm⁶/m²) cases accounts for fewer than 2% of all available Summit
27 MMCR data (4% if limited to JJA), and the LWP and PWV adjustments are -1.3 g/m² and
28 0.044 cm, respectively, for Z_{PATH} of 10^4 mm⁶/m². Thus the impact of the LWP bias on
29 seasonal statistics will be minimal. However an accurate LWP retrieval in the presence of ice
30 is important for precipitation specific cases. In addition, the small number of high Z_{PATH} cases
31 represent the heaviest snowfalls and thus are important for capturing the annual snowfall
32 (Castellani *et al.*, 2015).

1 The multi-frequency relationships in the high frequency MWR channels, illustrated in our
2 results in Sect. 5.3, show a linear relationship between the 90 GHz channel versus both the
3 150 and 225 GHz channels and increasing Z_{PATH} values as a function of larger BT differences
4 in each case. The initial SOI model runs for a synthetic ice cloud agree well with the
5 observations, in both the relative slope and in Z_{PATH} magnitude. These results can also act as
6 a starting point to a more rigorous LWP and PWV correction as described in Sect. 5.5. In
7 future work, it may be possible to combine the MWRRET algorithm with data from the
8 MMCR to create a robust joint retrieval of the LWP and the microwave ice signature. This
9 will recover data at the large Z_{PATH} values and should lead to unbiased retrievals of LWP and
10 PWV directly. Ultimately, a joint retrieval of LWP, PWV, and Ice Water Path (IWP) is
11 desired.

12 To accurately retrieve IWP from the measured ice signature, we need accurate descriptions of
13 the ice habit, surface temperature and emissivity, and ice PSDs more representative of
14 conditions at Summit. For future work, we hope to employ a PSD with a better fit to the
15 Summit conditions and eventually have ICECAPS instrumentation capable of measuring a
16 PSD *in-situ*. The measured ice signature technique outlined in this work is a novel approach
17 to better understand ice hydrometeors and could prove to be a powerful tool in future ground
18 and remote sensing applications.

19 **Acknowledgements**

20 ICECAPS and associated research in this study is supported by NSF PLR1304544,
21 PLR1355654, and PLR1303879. Partial support is also provided by NASA NNX12AQ76G
22 and NNX13AG47G. We appreciate the advice and contributions from Dr. Stefan Kneifel, the
23 use of the ASIAA MWR at Summit Station (P.I. Dr. Ming-Tang Chen), our colleague Dr.
24 Von Walden, and all the technicians and support staff that keep the ICECAPS suite running.
25 Ceilometer measurements were provided by the US Department of Energy's Atmospheric
26 Radiation Measurement Program.

27

1 **References**

- 2 Ackerman, T. P. and Stokes, G. M.: The Atmospheric Radiation Measurement Program,
3 *Physics Today*, 55, 39-44, 2003.
- 4 Bennartz R. and Petty, G. W.: The Sensitivity of Microwave Remote Sensing Observations
5 of Precipitation to Ice Particle Size Distributions, *Journal of Applied Meteorology*, 40, 345-
6 364, 2001.
- 7 Bennartz, R. and Bauer, P.: Sensitivity of microwave radiances at 85–183 GHz to
8 precipitating ice particles, *Radio Science*, 38, 8075, doi:10.1029/2002RS002626, 2003.
- 9 Castellani, B. B., Shupe, M. D., Hudak, D. R., and Sheppard, B. E.: The annual cycle of
10 snowfall at Summit, Greenland, *Journal of Geophysical Research*, 120, 6654–6668. doi:
11 10.1002/2015JD023072, 2015.
- 12 Church, J. A.: Changes in sea level, *Climate Change 2001: The Scientific Basis*. Cambridge
13 University Press, 639–693, 2001.
- 14 Crewell, S. and Löhnert, U.: Accuracy of cloud liquid water path from ground-based
15 microwave radiometry 2. Sensor accuracy and synergy, *Radio Science*, 38, 8042-8051.
16 doi:10.1029/2002RS002634, 2003.
- 17 Crewell, S., Ebell, K., Löhnert, U., and Turner, D. D.: Can liquid water profiles be retrieved
18 from passive microwave zenith observations? *Geophysical Research Letters*, 36, L06803.
19 doi:10.1029/2008GL036934, 2009.
- 20 Dansgaard, W., Johnsen, S. J., Clausen, H. B., Dahl-Jensen, D., Gundestrup, N. S., Hammer,
21 C. U., Hvidberg, C. S., Steffensen, J. P., Sveinbjörnsdottir, A. E., Jouzel, J., and Bond, G.:
22 Evidence for general instability of past climate from a 250-kyr ice-core record. *Nature*, 364,
23 218-220, 1993.
- 24 Deeter, Merritt N., and K. Franklin Evans.: A novel ice-cloud retrieval algorithm based on the
25 Millimeter-Wave Imaging Radiometer (MIR) 150-and 220-GHz channels, *Journal of Applied*
26 *Meteorology*, 39 (5), 623-633, 2000.
- 27 Field, P. R., Hogan, R. J., Brown, P. R. A., Illingworth, A. J., Choullarton, T. W., and Cotton,
28 R.: Parameterization of ice-particle size distributions for mid-latitude stratiform cloud,
29 *Quarterly Journal of the Royal Meteorological Society*, 131, 1997-2017, doi:10.1256/qj.04.134,
30 2005.

1 Field, P. R., Heymsfield, A. J., and Bansmer, A.: Snow Size Distribution Parameterization for
2 Midlatitude and Tropical Ice Clouds, *Journal of the Atmospheric Sciences*, 64, 4346-4365,
3 2007.

4 Frisch, A. D., Lenschow, D. H., Fairall, C. W., Schubert, W. H., and Gibson, J. S.: Doppler
5 Radar Measurements of Turbulence in Marine Stratiform Cloud during ASTEX, *Journal of*
6 *the Atmospheric Sciences*, 52, 2800-2808, 1995.

7 Garrett, T. J., Fallgatter, C., Shkurko, K., and Howlett, D.: Fall speed measurement and high-
8 resolution multi-angle photography of hydrometeors in free fall, *Atmospheric Measurement*
9 *Techniques*, 5, 2625-2633, 2012.

10 Heidinger, A. K., O'Dell, C. W., Bennartz, R., and Greenwald, T.: The Successive-Order-of-
11 Interaction Radiative Transfer Model. Part I: Model Development, *Journal of Applied*
12 *Meteorology and Climatology*, 45, 1388-1402, 2006.

13 Hong G., Heygster, G., Miao, J., and Kunzi, K.: Detection of tropical deep convective clouds
14 from AMSU-B water vapor channels measurements, *Journal of Geophysical Research*, 110,
15 D05205, doi:10.1029/2004JD004949, 2005.

16 Johnson, B. T., Petty, G. W., and Skofronick-Jackson, G.: Microwave Properties of Ice-Phase
17 Hydrometeors for Radar and Radiometers: Sensitivity to Model Assumptions, *Journal of*
18 *Applied Meteorology and Climatology*, 51, 2152-2171, 2012.

19 Kneifel, S., Löhnert, U., Battaglia, A., Crewell, S., and Siebler, D.: Snow scattering signals in
20 ground based passive microwave radiometer measurements, *Journal of Geophysical Research*,
21 115, D16214, doi:10.1029/2010JD013856, 2010.

22 Kneifel, S., Bennartz, R., and Kulie, M. S.: A triple-frequency approach to retrieve
23 microphysical snowfall parameters, *Journal of Geophysical Research*, 116, D11203,
24 doi:10.1029/2010JD015430, 2011.

25 Kulie, M. S. and Bennartz, R.: Utilizing space-borne radars to retrieve dry snowfall, *Journal*
26 *of Applied Meteorology and Climatology*, 48, 2564–2580, doi:10.1175/2009JAMC2193.1,
27 2009.

28 Kulie, M. S., Bennartz, R., Greenwald, T., Chen, Y., and Weng, F.: Uncertainties in
29 Microwave Properties of Frozen Precipitation: Implications for Remote Sensing and Data
30 Assimilation, *Journal of Atmospheric Science*, 67, 3471-3487, 2010.

1 Liebe, H., Hufford, G., and Manabe, T.: A model for the permittivity of water at frequencies
2 below 1THz, *International Journal of Infrared Millimeter and Terahertz Waves*, 12, 659-675,
3 1991.

4 Liu, G.: A database of microwave single-scattering properties for nonspherical ice particles,
5 *Bulletin of the American Meteorological Society*, 89, 1563-1570, 2008.

6 Löhnert, U. and Crewell, S.: Accuracy of cloud liquid water path from ground-based
7 microwave radiometry, 1, Dependency on cloud model statistics, *Radio Science*, 38(3), 8041,
8 doi:10.1029/2002RS002654, 2003.

9 Matsushita, S., Chen, M., Martin-Cocher, P., Asada, K., Chen, C., Inoue, M., Paine, S.,
10 Turner, D. D., and Steinbring, E.: 225 GHz Atmospheric Opacity Measurements from Two
11 Arctic Sites, *Astrophysics from Antarctica Proceedings IAU Symposium*,
12 doi:10.1017/S1743921312016882, 2013.

13 Moran, K. P., Martner, B., Post, M. J., Kropfli, R. A., Welsh, D. C., and Widener, K. B.: An
14 unattended cloud-profiling radar for use in climate research, *Bulletin of the American*
15 *Meteorological Society*, 79, 443–455, 1998.

16 O’Dell, C. W., Heidinger, A. K., Greenwald, T., Bauer, P., and Bennartz, R.: The Successive-
17 Order-of-Interaction Radiative Transfer Model. Part II: Model Performance and Applications,
18 *Journal of Applied Meteorology and Climatology*, 45, 1403-1413, 2006.

19 Petty, G. W. and Huang, W.: Microwave backscatter and extinction by soft ice spheres and
20 complex snow aggregates, *Journal of Atmospheric Science*, 67, 769-787, 2010.

21 Pruppacher, H. R. and Klett, J. D.: *Microphysics of clouds and precipitation*. Kluwer
22 Academic Publishers, The Netherlands, 2000.

23 Rose, T., Crewell, S., Löhnert, U., and Simmer, C.: A network suitable microwave radiometer
24 for operational monitoring of the cloudy atmosphere, *Atmospheric Research*, 75, 183-200,
25 doi:10.1016/j.atmosres.2004.12.005, 2005.

26 Shupe, M. D., Walden, V. P., Eloranta, E., Uttal, T., Campbell, J. R., Starkweather, S. M., and
27 Shiobara, M.: Clouds at Arctic atmospheric observatories, Part I. Occurrence and
28 macrophysical properties, *Journal of Applied Meteorology and Climatology*, 50, 626-644,
29 2011.

1 Shupe, M. D., Turner, D. D., Walden, V. P., Bennartz, R., Cadeddu, M., Castellani, B. B.,
2 Cox, C. J., Hudak, D. R., Kulie, M. S., Miller, N. B., Neely, R. R., Neff, W. D., and Rowe, P.
3 M.: High and Dry: New Observations of Tropospheric and Cloud Properties above the
4 Greenland Ice Sheet, *Bulletin of the American Meteorological Society*, 94(2), 169-186, 2013.

5 Turner, D. D., Lesht, B. M., Clough, S. A., Liljegren, J. C., Revercomb, H. E., and Tobin, D.
6 C.: Dry bias and variability in Vaisala radiosondes: The ARM experience, *Journal of*
7 *Atmospheric and Oceanic Technology*, 20, 117-132, 2003.

8 Turner, D. D., Clough, S. A., Liljegren, J. C., Clothiaux, E. E., Cady-Pereira, K., and Gaustad,
9 K. L.: Retrieving Liquid Water Path and Precipitable Water Vapor From the Atmospheric
10 Radiation Measurement (ARM) Microwave Radiometers, *IEEE Transactions on Geoscience*
11 *and Remote Sensing*, 45, 3680-3690, 2007a.

12 Turner, D. D., Vogelmann, A. M., Austin, R. T., Banard, J., Cady-Pereira, K., Chiu, J. C.,
13 Clough, S. A., Flynn, C., Khaiyer, M. M., Liljegren, J. C., Johnson, K., Min, Q., Minnis, P.,
14 O'Hirok, W., Wang, Z., and Wiscombe, W.: Thin liquid water clouds: Their importance and
15 our challenge, *Bulletin of the American Meteorological Society*, 88, 177-190, 2007b.

16 Turner, D. D.: Improved ground-based liquid water path retrievals using a combined infrared
17 and microwave approach, *Journal of Geophysical Research*, 112, doi:10.1029/2007JD008530,
18 2007c.

19 Turner, D. D., Kneifel, S., and Cadeddu, M.: An improved liquid water absorption model in
20 the microwave for supercooled liquid water clouds, *Journal of Atmospheric and Oceanic*
21 *Technology*, 33, 33-44, doi:10.1175/JTECH-D-15-0074.1, 2015.

22 Uttal, T., and 53 coauthors.: International Arctic systems for observing the atmosphere
23 (IASOA): An international polar year legacy consortium. *Bulletin of the American*
24 *Meteorological Society*, submitted, 2015.

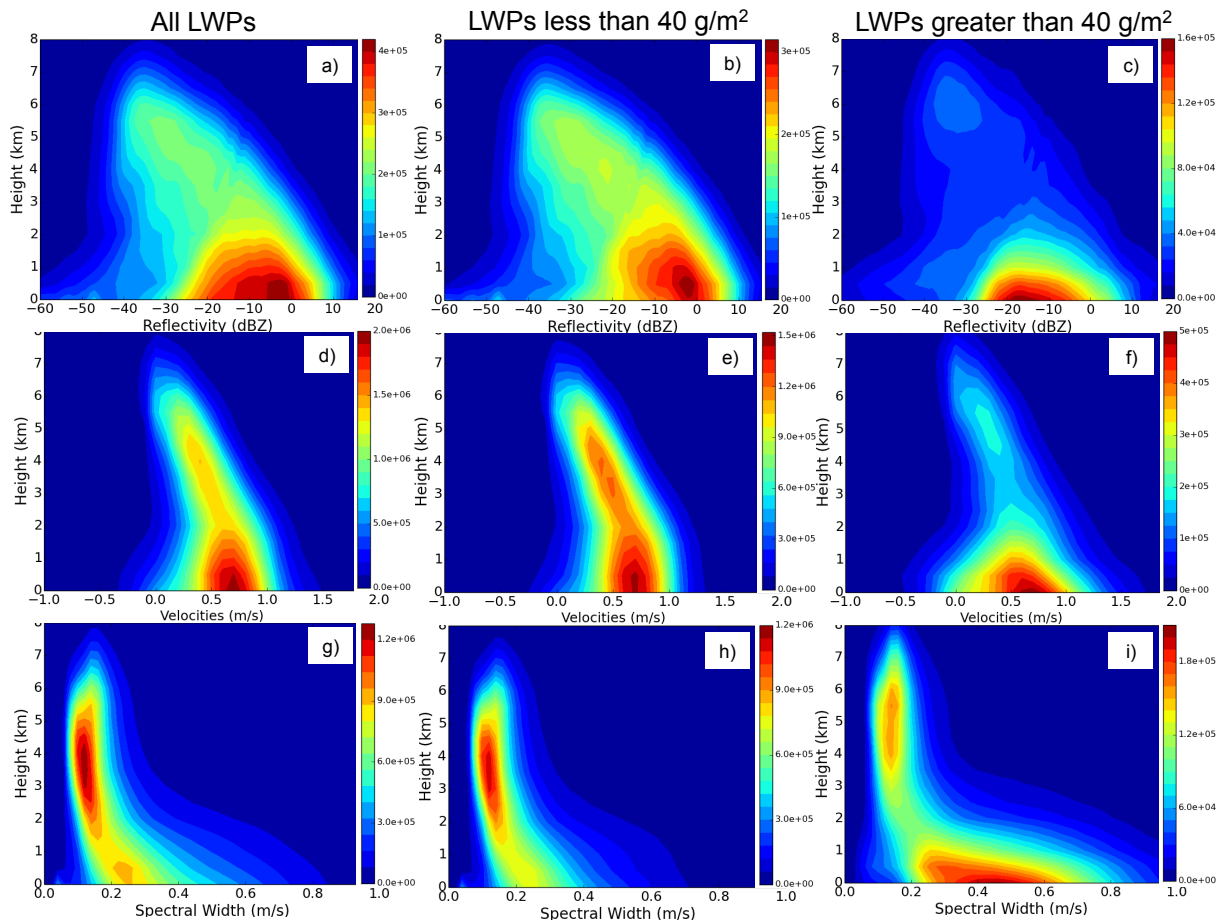
25 Yan, B., Weng, F., and Meng, H.: Retrieval of snow surface microwave emissivity from the
26 advanced microwave sounding unit, *Journal of Geophysical Research*, 113, D19206,
27 doi:10.1029/2007JD009559, 2008.

28

1 Table 1. Sub-group of ICECAPS suite instruments used in this study (modified from Table 1
 2 in Shupe *et al.* 2013).

Instrument Name	Specifications	Measurements	Derived Parameters
HATPRO	Frequencies: 22-32 GHz (7 channels) 51-58 GHz (7 channels) 2 to 4-second resolution	Downwelling Brightness Temperature	Cloud LWP and PWV
MWRHF	Frequencies: 90 and 150 GHz. 2 to 4-second resolution	Downwelling Brightness Temperature	Cloud LWP and PWV
MMCR	35 GHz (Ka band), 8-mm wavelength. 45-meter vertical bin size. 2-second resolution	Reflectivity, Doppler velocity, Doppler spectral width	Cloud micro and macro-physics Cloud dynamics
Ceilometer	905nm wavelength, 15-meter vertical resolution. 15-second resolution.	Backscatter	Cloud-base height
RS-92K or RS-92SGP Radiosondes	Twice daily (00 and 12Z) 1-second resolution.	Temperature, relative humidity, pressure, winds	Cloud temperature, tropospheric thermodynamic structure
MWRHF-225	Frequency: 225 GHz. 4-second resolution.	Downwelling Brightness Temperature	Atmospheric opacity

3

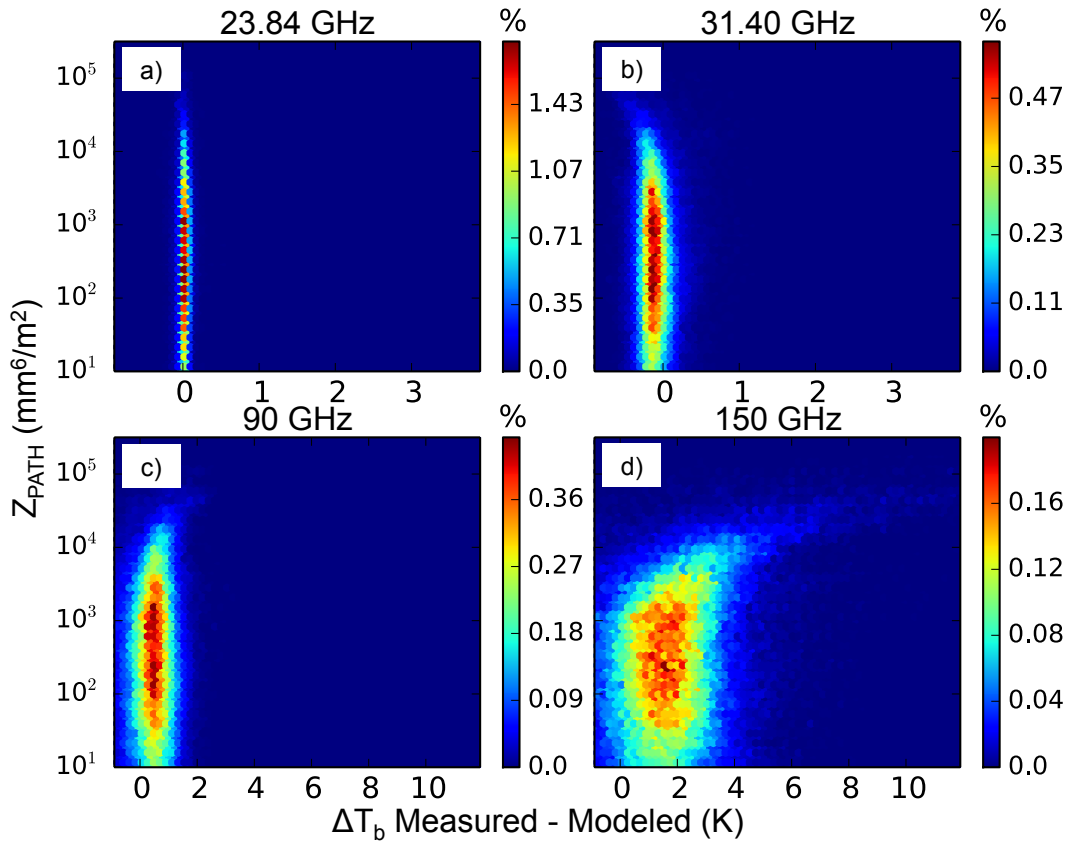


1

2

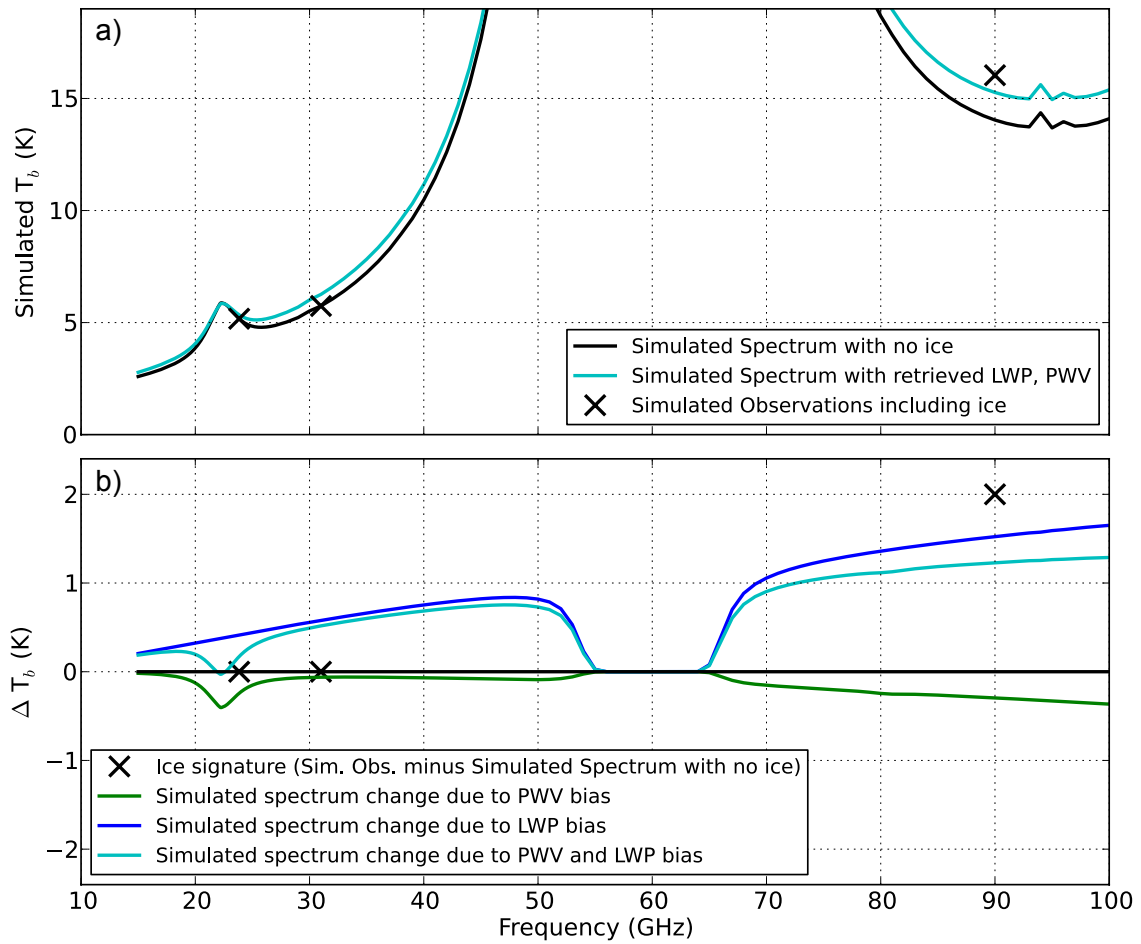
3 Figure 1. CFADs of MMCR reflectivity for summer (JJA) at Summit, Greenland from June
 4 2010 through August 2013 with a sample resolution rate every 10 seconds. Panel a) shows
 5 JJA reflectivity for all measured LWPs while panel b) is filtered to reflectivities only when
 6 LWP is less than 40g/m^2 and panel c) is filtered for cases greater than 40g/m^2 . Additional
 7 CFADs of MMCR Doppler velocity and spectral width for summer at Summit, Greenland for
 8 all LWPs (panels d and g), when LWP is less than 40g/m^2 (panels e and h), and when LWP is
 9 greater than 40g/m^2 (panels f and i), respectively. LWP less than 40g/m^2 accounted for
 10 $\sim 63\%$ of cases, while greater than 40g/m^2 is 22% of cases, and the remaining 15% is clear
 11 sky (as determined by the MMCR).

Brightness Temperature Differences for JJA with LWP less than 40g/m²



1
2

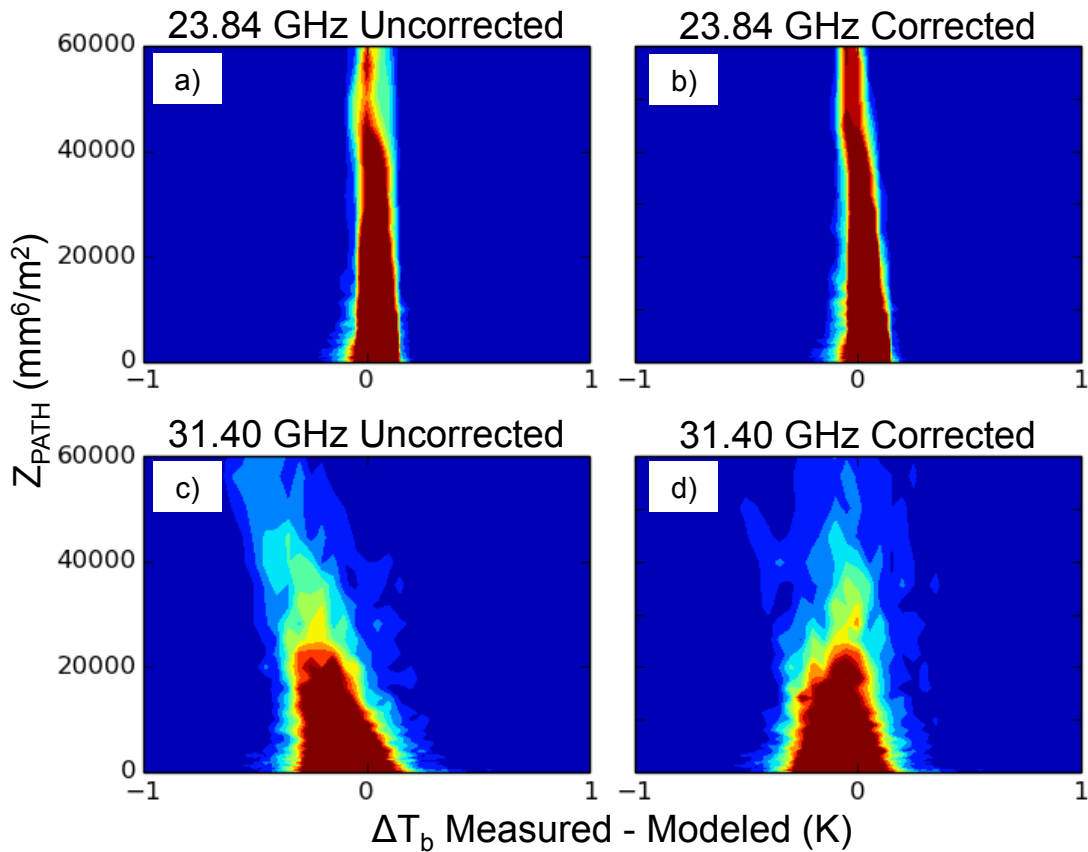
3 Figure 2. Brightness temperature differences between observations minus the modelled gas
 4 and liquid contributions in the 23.84, 31.40, 90, and 150 GHz channels as a function of Z_{PATH}
 5 for LWP less than 40 g/m². The count histogram is binned logarithmically in Z_{PATH} and
 6 linearly in ΔT_b , shown as percentage of total observation count per bin. The 150 GHz channel
 7 shows an enhanced BT difference with respect to Z_{PATH} (panel d), while the 90 GHz has a
 8 slight enhanced BT, the 31 GHz exhibits a negative dependence, and the 23.84 GHz is
 9 channel neutral.



1

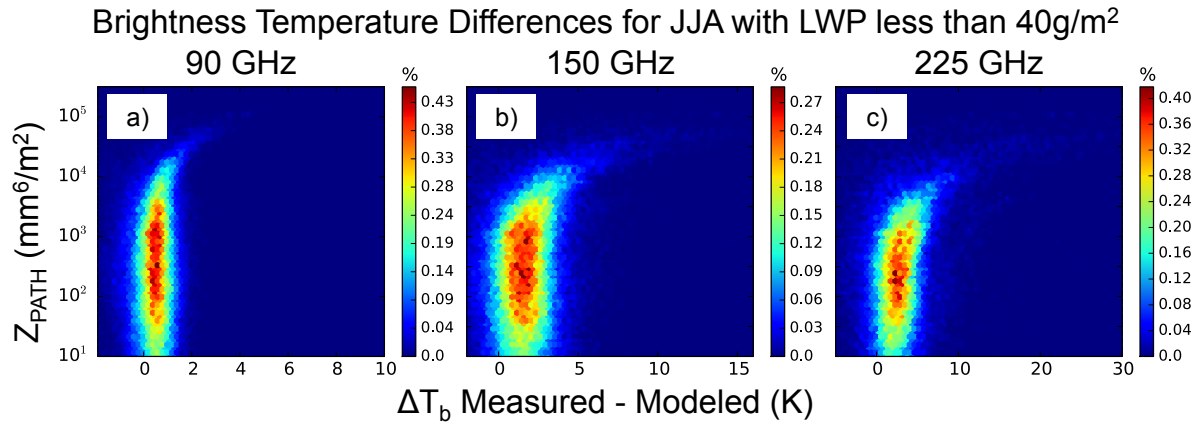
2

3 Figure 3. Panel a shows the simulated downwelling microwave radiance spectrum with no ice
 4 (black) and the simulated spectrum with the biased PWV and LWP obtained by the retrieval
 5 (cyan). Panel b shows the simulated data after subtracting the simulated spectrum with no ice.
 6 The effect of the biased LWP and PWV on the microwave spectrum are shown independently
 7 (blue and green lines, respectively) and combined (cyan line). The “X” marks show the
 8 simulated ice influence at 23.84, 31.40, and 90 GHz.



1
2
3
4
5
6
7
8
9
10
11
12

Figure 4. Histograms of the MMCR Z_{PATH} and the difference between the measured and modeled BT at 23.84 and 31.40 GHz before and after the linear correction are shown above. Contour levels are linearly spaced, showing counts per factor of $10^{0.05}$ in Z_{PATH} and per 0.05 K in BT difference. The y-axis is truncated to 6×10^4 mm^6/m^2 Z_{PATH} to highlight the correction in the low ice optical depth cases. Red signifies 50 and higher counts and blue signifies fewer than 5 counts. Plots are linear in both axes. The uncorrected 31.40 GHz channel (panels c) has a negative bias as a function of the Z_{PATH} . The slope of the uncorrected 31.40 GHz (panel c) histogram yields the value of $\Delta T_b / \Delta Z_{PATH}$ used in the linear correction. For both low frequency channels, once the correction is applied, no dependence on Z_{PATH} is present (panels b and d).

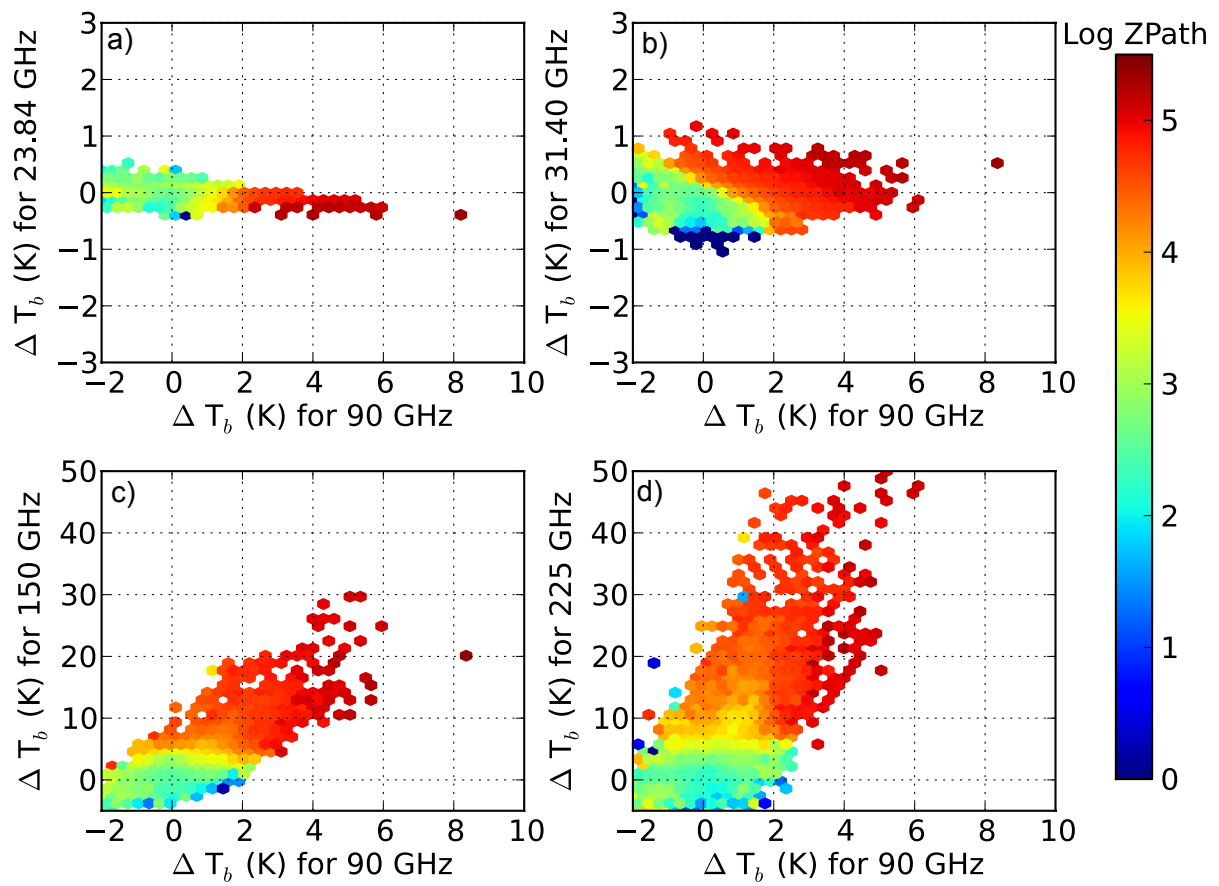


1

2

3 Figure 5. Brightness temperature differences between the HFMWR and the HFMWR-225
 4 observations and the modelled gas and liquid contributions after implementing the LWP
 5 correction for ice for the 90, 150, and 225 GHz channels. The count histogram is binned
 6 logarithmically in Z_{PATH} and linearly in ΔT_b , shown as percentage of total observation count
 7 per bin (same as Figure 2). The high frequency channels show a dependence of the difference
 8 in brightness temperature and the Z_{PATH} from the MMCR – thus, indicating an increasing
 9 brightness temperature in these channels with increasing total ice amount in the column.
 10 Additionally, the sensitivity to the ice signature increases as a function of higher frequency.
 11 The Z_{PATH} value where the ice signature BT enhancement begins is lower in the 150 versus
 12 the 90 GHz channel (panels b and c, respectively) and lowest in the 225 GHz (panel c). We
 13 note that there is a clear sky bias in all three channels, but the magnitude of this bias is smaller
 14 than the radiometric uncertainty of the HFMWR observations. We are unable at this time to
 15 determine if this bias is due to calibration uncertainty in the radiometer or the result of
 16 forward model error.

Multi-frequency Comparisons – JJA with LWP less than 40 g/m²

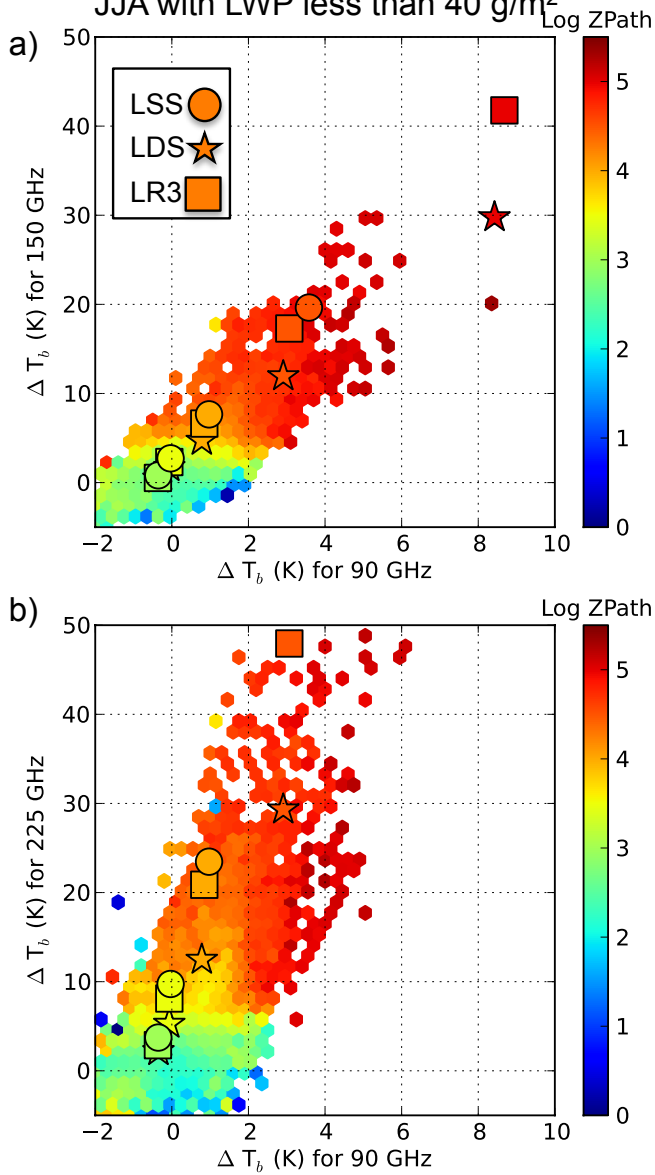


1

2

3 Figure 6. Multi-frequency plots of the BT difference in channels 23.84, 31.40, 150, and 225
4 GHz as compared to the 90 GHz channel. The binned values of BT difference are coloured
5 according to logarithm of the average Z_{PATH} values. In the top two panels, the lower
6 frequency channels are plotted against 90 GHz (a and b) and in the bottom two panels, the
7 150 and 225 GHz are plotted against the 90 GHz (c and d).

Multi-frequency Comparisons with SOI Simulations –
 JJA with LWP less than 40 g/m²



1

2

3 Figure 7. SOI simulated BT differences plotted on top of the observations for the 150 versus
 4 90 GHz and 225 versus 90 GHz channels (panel a and b, respectively). In both examples, the
 5 slopes of the simulations agree well with the observations.